Published online 6 June 2018

Nucleic Acids Research, 2018, Vol. 46, No. 12 ***6371–6386***
doi: 10.1093/nar/gky469

Functional insights into the *Streptococcus pneumoniae* HicBA toxin–antitoxin system based on a structural study

Do-Hee Kim[1,†], Sung-Min Kang[1,†], Sung Jean Park[2], Chenglong Jin[1], Hye-Jin Yoon[3] and Bong-Jin Lee[1,*]

[1]The Research Institute of Pharmaceutical Sciences, College of Pharmacy, Seoul National University, Gwanak-gu, Seoul 08826, Republic of Korea, [2]College of Pharmacy and Gachon Institute of Pharmaceutical Sciences, Gachon University, 534-2 Yeonsu-dong, Yeonsu-gu, Incheon 13120, Republic of Korea and [3]Department of Chemistry, College of Natural Sciences, Seoul National University, Seoul 08826, Republic of Korea

Received December 19, 2017; Revised May 09, 2018; Editorial Decision May 10, 2018; Accepted May 15, 2018

ABSTRACT

Streptococcus pneumonia **has attracted increasing attention due to its resistance to existing antibiotics. TA systems are essential for bacterial persistence under stressful conditions such as nutrient deprivation, antibiotic treatment, and immune system attacks. In particular, *S. pneumoniae* expresses the HicBA TA gene, which encodes the stable HicA toxin and the labile HicB antitoxin. These proteins interact to form a non-toxic TA complex under normal conditions, but the toxin is activated by release from the antitoxin in response to unfavorable growth conditions. Here, we present the first crystal structure showing the complete conformation of the HicBA complex from *S. pneumonia*. The structure reveals that the HicA toxin contains a double-stranded RNA-binding domain that is essential for RNA recognition and that the C-terminus of the HicB antitoxin folds into a ribbon-helix-helix DNA-binding motif. The active site of HicA is sterically blocked by the N-terminal region of HicB. RNase activity assays show that His36 is essential for the ribonuclease activity of HicA, and nuclear magnetic resonance (NMR) spectra show that several residues of HicB participate in binding to the promoter DNA of the HicBA operon. A toxin-mimicking peptide that inhibits TA complex formation and thereby increases toxin activity was designed, providing a novel approach to the development of new antibiotics.**

INTRODUCTION

Streptococcus pneumoniae is a gram-positive, facultative anaerobic bacterium and a significant human pathogen that causes otitis media, sinusitis, pneumonia and meningitis. *Streptococcus pneumoniae* is usually inhaled into the respiratory system and remains in the pharynx and nasal cavity, where it may cause diseases (1,2). Glycopeptide antibiotics such as vancomycin and as penicillin are frequently used to eradicate the bacteria and relieve symptoms (3,4). However, substantial evidence of antibiotic resistance in *S. pneumoniae* has accumulated worldwide. Unfortunately, extensively drug-resistant *S. pneumoniae* with resistance to penicillin, cephalosporin, macrolides, β-lactam antibiotics, fluoroquinolone and even vancomycin and linezolid have appeared (5–7). Currently, antibiotic combination therapy is used to obtain synergistic treatment effects, but it cannot effectively suppress the growth of drug-resistant bacteria (8–10). Therefore, the development of new antibiotic candidates to eradicate *S. pneumoniae* by exploiting new therapeutic strategies is urgently needed.

In bacteria, toxin–antitoxin (TA) systems are strongly correlated with physiological processes such as gene regulation, growth arrest, survival and apoptosis (11–15). TA loci were first discovered in 1983 on the mini-F plasmid of *Escherichia coli*, a plasmid addiction module that is responsible for the maintenance of extrachromosomal genetic elements (16). TA systems consist of toxin genes and antitoxin genes. TA systems are typically located on bacterial plasmids and transferred to daughter cells to yield plasmid stabilization and cell viability (17,18). In contrast, TA systems located on chromosomes are commonly related to growth arrest, biofilm formation and multidrug tolerance and facilitate the development of persister or dormant cells (19–22).

*To whom correspondence should be addressed. Tel: +82 2 880 7869; Fax: +82 2 872 3632; Email: lbj@nmr.snu.ac.kr
†The authors wish it to be known that, in their opinion, the first two authors should be regarded as Joint First Authors.

© The Author(s) 2018. Published by Oxford University Press on behalf of Nucleic Acids Research.
This is an Open Access article distributed under the terms of the Creative Commons Attribution Non-Commercial License (http://creativecommons.org/licenses/by-nc/4.0/), which permits non-commercial re-use, distribution, and reproduction in any medium, provided the original work is properly cited. For commercial re-use, please contact journals.permissions@oup.com

A toxin damages the host cell by inhibiting DNA replication, protein synthesis and cell wall synthesis by degrading host RNA or by binding to topoisomerases or ribosomes (23–25). In contrast, an antitoxin is an important cellular component because it neutralizes the detrimental activity of its cognate toxin (26).

TA systems are classified into five groups that are referred to as types I–V. In type I TA systems, the antitoxin is an antisense RNA that binds to the toxin mRNA. The antitoxin inhibits the translation of the toxin and causes it to be degraded. In type II TA systems, both the toxin and the antitoxin are proteins that interact with each other to form a non-toxic protein complex. In type III TA systems, the antitoxin is an RNA that binds directly to the toxin protein to form a non-toxic RNA–protein complex. In type IV TA systems, the toxin and antitoxin do not bind directly to each other but instead compete for the same cellular target. In type V TA systems, the antitoxin is a protein that degrades the toxin mRNA to prevent its expression (27–31). HicBA is a type II TA system. In type II TA systems, the toxin is thermodynamically stable, whereas the antitoxin is unstable and is cleaved by cellular proteases because its locally flexible conformation makes it susceptible to proteolysis. Upon proteolysis of the antitoxin, the free toxin is released from the TA complex and binds to host cell components, causing growth arrest or even death of the host cell (32–34).

The *S. pneumoniae* strain TIGR4 contains only six TA loci (three RelBE family, one phd-doc family, one HigBA family and one HicBA family) (35). Overall, *S. pneumoniae* contains a small number of TA loci relative to other bacteria. For example, *Mycobacterium tuberculosis* possesses more than 88 known TA operons. Although the mechanisms of TA activity have been studied for a long time, the physiological roles of TA have not yet been clearly elucidated (36–38). Furthermore, the only HicBA TA complex crystal structure determined to date is that of *Yersinia pestis*, Protein Data Bank (PDB) code 4P78 (HicBA3), which lacks the C-terminal region of the antitoxin (39).

HicB antitoxins consist of two functional motifs: an N-terminal region that binds to the toxin and thereby abolishes its toxicity and a C-terminal region that regulates its TA operon by binding to tis promoter DNA (40,41). The DNA-binding domain of HicB (42) forms a ribbon-helix-helix (43) or helix-turn-helix motif (44). HicA toxins contain a double-stranded RNA binding domain (45) and exhibit ribonuclease activity (46). The active sites of HicA toxins contain a conserved histidine residue (39,47).

Here, we present the crystal structure of the HicBA complex of *S. pneumoniae* TIGR4 at a resolution of 2.30 Å. The C-terminal DNA-binding domain of the HicB antitoxin shows considerable structural variation, and the HicA toxin forms contacts with the curved back of the HicB antitoxin. This structure reveals the residues that are important in the formation of the HicBA complex. The core residues in HicB that bind to DNA and the properties of the DNA-binding domain were elucidated by nuclear magnetic resonance (NMR). As antibiotic candidates, binding interface-mimicking peptides were designed to act as antimicrobial peptides that suppress the TA interaction. This approach may contribute to the development of novel potent antibiotics as effective treatments for antibiotic-resistant *S. pneumoniae*.

MATERIALS AND METHODS

Cloning and transformation

The genes encoding HicB (*SP1786*) and HicA (*SP1787*) were amplified by the polymerase chain reaction (PCR). The primers used in PCR were HicB-F/HicB-R (for HicB) and HicA-F/HicA-R (for HicA) (Supplementary Table S1A). The restriction enzymes used for cloning were Nde1 and Xho1. The PCR products of both HicB and HicA were double-cut by Nde1 and Xho1 and ligated into vectors that had been cut by the same enzymes. For structure determination and biological assays, HicB and HicA were ligated into pET21a with no tag and into pET28b, respectively. The pET28b N-terminal tag (MGSSHHHHHHSSGLVPRGSH) was added to HicA as an additional residual tag. For the NMR experiments, the residues of HicB including the DNA-binding domain ($HicB^{109–150}$) were cloned. The primers used in PCR were $HicB^{109–150}$-F and HicB-R (Supplementary Table S1A). Restriction digestion was conducted in the same way, and pET28b was used for ligation with the same tag. To confirm the identity of the residue essential to the ribonuclease activity of HicA, His36 of HicA was mutated to Ala36 (HicA-H36A). The primers used in PCR were H36A-F/H36A-R (Supplementary Table S1A). Mutation was conducted using the EZchange™ Site-Directed Mutagenesis Kit (Enzynomics, Korea) according to the manufacturer's protocol.

Protein expression and purification

The cloned plasmids containing HicB and HicA were co-transformed into *E. coli* Rosetta2 (DE3) pLysS competent cells. The cells were grown at 37°C in Luria broth (LB) until the OD_{600} of the cell suspension reached 0.8. Protein overexpression was induced by the addition of 0.5 mM isopropyl 1-thio-β-D-galactopyranoside (IPTG), and incubation at 37°C was continued for 4 h. The cultured cells were harvested by centrifugation at 11 355 × g at 4°C and stored at –80°C. The harvested cells were suspended in buffer A (20 mM Tris–HCl, pH 7.9, and 500 mM NaCl) containing 5% glycerol by volume and lysed by ultrasonication. After centrifugation for 1 h at 28 306 × g, the supernatant containing soluble proteins was loaded onto a Ni^{2+} affinity open column (Bio-Rad) that had been equilibrated with buffer A, and the column was washed with buffer A containing 50 mM imidazole. The protein bound to the Ni^{2+} column was eluted using an imidazole gradient (100−700 mM), and the TA complex in each fraction was identified using sodium dodecyl sulfate polyacrylamide gel electrophoresis (SDS-PAGE). Finally, the buffer containing the TA complex was exchanged for buffer consisting of 20 mM Tris, pH 7.5 and 150 mM NaCl by size-exclusion chromatography on a HiLoad 16/600 Superdex 200 prep-grade column (GE Healthcare) and concentrated to 10 mg/ml using an Amicon Ultra centrifugal filter unit (Millipore). The purity of the TA protein complex was verified by SDS-PAGE. For the ribonuclease assay, HicA and

HicA-H36A were expressed and purified by the same procedure except that HicA-expressing cells were incubated for only 2 h after IPTG induction because of the toxicity of the protein to *E. coli*. The HicBA complex labeled with selenomethionine (SeMet) was obtained by the same procedure, except that cells containing the SeMet-labeled HicBA complex were grown in M9 medium containing extra essential amino acids. For the NMR experiments, the N-terminal $(His)_6$-tagged $HicB^{109–150}$ protein was expressed in *E. coli* strain BL21(DE3) using M9 medium mixed with 1.0 g/l [U-^{13}C] glucose and 1.0 g/l [^{15}N] NH_4Cl (Cambridge Isotopes Laboratory) as the sole carbon and nitrogen sources, respectively. The purification of $HicB^{109–150}$ was the same as for the TA complex. To cleave the $(His)_6$ tag prior to size-exclusion chromatography, 100 units of thrombin from human plasma (Sigma-Aldrich) were added to 10 mg of purified protein and incubated overnight at 20°C in a buffer consisting of 20 mM sodium phosphate (Na Pi), pH 7.0, and 100 mM NaCl. VapC26 and VapC30 from *M. tuberculosis* were expressed and purified as reported previously (48,49).

Crystallization, data collection and processing

Initial crystal screening of the purified HicBA complex was conducted using the Crystal Screening 1, 2 and Index (Hampton Research) kits by mixing 1 μl of protein solution at 10 mg/ml in 20 mM Tris, pH 7.5 and 150 mM NaCl with 1 μl of reservoir solution. Crystals of the HicBA complex were grown using the sitting-drop vapor diffusion method at 4°C. The crystallization solution for HicBA was 0.1 M Tris, pH 8.5 and 2.0 M ammonium sulfate. Cryoprotection of HicBA was achieved by adding 20% glycerol to the solution. The crystals were flash-cooled in liquid nitrogen prior to data collection. The data were collected using an ADSC Quantum Q270r CCD detector at beamlines 5C and 7A of the Pohang Light Source, Republic of Korea. The crystals of the HicBA complex belong to the *orthorhombic* space group $P2_12_12$ and display unit cell parameters of $a = 106.263$ Å, $b = 116.541$ Å, $c = 42.490$ Å, and $\alpha = \beta = \gamma = 90.00°$ for the native HicBA crystal and $a = 106.926$ Å, $b = 116.602$ Å, $c = 42.680$ Å, and $\alpha = \beta = \gamma = 90.00°$ for the SeMet-labeled crystals. The calculated total mass of the protein complex, including the N-terminal histidine tag was 26349.7 Da. All raw data were scaled and processed by the HKL2000 (50). The structure of the HicBA complex from *S. pneumoniae* was determined at 2.80 Å resolution by single-wavelength anomalous dispersion using SeMet-labeled crystals. The final structure of HicBA was determined by molecular replacement. The 2.30 Å data on the native crystal were used for structural analysis, and the SeMet structure was used as a model to determine the native structure. Detailed statistical information on the structures is provided in Supplementary Table S2. In the SeMet structure, we determined the positions of 14 selenium sites in the asymmetric unit. *PHENIX* (51) was first used to automatically build the model, and *COOT* (52) was utilized to provide the starting model for refinement. R_{work}/R_{free} values (53) of the SeMet and the native final models using *REFMAC* and *PHENIX* (51,54) were 20.2/24.0% and 20.5/23.6%, respectively. The overall geometry was validated using *MolProbity* (55), the results showed that 98% of the residues were in the favored region of the Ramachandran plot and an additional 2% were in the allowed region in the native structure. PyMOL was used to generate all figures (56). The electrostatic potential surfaces were calculated using the Adaptive Poisson-Boltzmann solver (APBS) method (57).

Size-exclusion chromatography coupled with multi-angle light scattering (SEC-MALS)

MALS was performed to determine the oligomeric states of HicBA. Size-exclusion chromatography was conducted on a BioSep SEC-s3000 column (Phenomenex) on a 1260 Infinity HPLC system (Agilent Technologies). The scattering data were obtained in a miniDAWN-TREOS line for emission at 657.4 nm (Wyatt Technology) and analyzed using ASTRA 6.0.1.10 software (Wyatt Technology). HicBA hetero-dimer at a concentration of 100 μM was used in the experiment, which was performed in 20 mM Tris, pH 7.5 and 150 mM NaCl, corresponding to the crystallization conditions. The experiments were performed at room temperature.

Electrophoretic mobility shift assay (EMSA)

EMSA was conducted to determine the binding affinity of HicB and HicBA to promoter DNA. A 28-base-pair DNA fragment from the upstream region (promoter DNA) of HicBA was added to the proteins as a palindromic form. The palindromic sequence was as follows: forward—TAAT AGAATAATAAGTATCACTCCTTTA; reverse—TAAA GGAGTGATACTTATTATTCTATTA. Two other palindromic sequences (Pal-I and Pal-II) and a control DNA ('X') were also prepared (Supplementary Table S1B). The annealed dsDNAs were purchased from Bioneer Innovation (http://www.bioneer.co.kr/). The dsDNAs and proteins were added to a binding buffer consisting of 20 mM Tris pH 7.5 and 150 mM NaCl, varying amounts of HicB and HicBA protein were then mixed with the DNA to yield a final volume of 10 μl and the mixtures were incubated for 20 min at 4°C. The total binding solutions were loaded onto 0.8% agarose gels in 0.5× TBE (45 mM Tris-borate, 1 mM EDTA) buffer, and the results were visualized using a Gel Doc (Bio-Rad).

Isothermal titration calorimetry (ITC) measurements

ITC experiments were performed at 25°C using a MicroCal 200 (GE Healthcare). HicB, HicBA and promoter dsDNA were prepared in a buffer consisting of 20 mM Tris, pH 7.5 and 150 mM NaCl. A dsDNA fragment from the upstream region (promoter DNA) of HicBA was added to the proteins. Affinity measurement was conducted at a protein concentration of 0.1 mM HicB dimer and 0.1 mM HicBA hetero-tetramer in a total volume of 320 μl using the promoter dsDNA solution (2 mM) as the injected titrant. Data collection was performed at 180-s intervals for a total of 19 injections. Curve fitting to calculate the binding affinity (K_d), the enthalpy of binding ($\triangle H$), the entropy of binding ($\triangle S$) and the molar ratio was performed using the MicroCal Origin software. The raw data were fitted to a one-site

binding model. The Gibbs free energies ($\triangle G$) were calculated using the standard equation $\triangle G = \triangle H - T\triangle S$.

NMR study of HicB$^{109–150}$ and DNA titration

NMR spectra of the HicB antitoxin were measured using a Bruker AVANCE DRX 800 spectrometer. All experiments were performed at 298 K. The samples were prepared in a buffer consisting of 20 mM NaPi, pH 7 and 100 mM NaCl containing 10% D_2O by total volume. The data were processed using NMRPipe/nmrDraw (58) and further analyzed using NMRviewJ (59). Data on the carbonyl carbon were obtained using the HNCO and HNCACO spectra, and data on the α/β carbon were acquired using the HNCACB and CBCACONH spectra. Additionally, to explore the structural transition in the ribbon-helix-helix domain that occurs during the binding of HicB to DNA, promoter DNA was added to HicB$^{109–150}$. DNA titration was conducted four times in the measurement of the ^{1}H,^{15}N-HSQC spectra. The concentration of HicB$^{109–150}$ monomer was maintained at 1 mM, and the DNA concentration was varied from 0 to 0.3 mM (a maximum of 30% of the protein concentration). The chemical shift perturbation (CSP) was calculated by nmrViewJ. The average CSP values of ^{15}N and ^{1}H were calculated from Equation (1), in which $\Delta\delta_N$ and $\Delta\delta_H$ represent the CSP values of the amide nitrogen and proton, respectively To determine K_d by NMR titration, the concentration of the HicB$^{109–150}$ monomer was maintained at 0.5 mM, and the DNA concentration was varied from 0 to 0.6 mM (a maximum of 120% of the protein concentration).

$$\Delta\delta_{avg} = [(0.2 \times \Delta\delta^2{}_N + \Delta\delta^2{}_H)/2]^{1/2} \quad (1)$$

In silico HicBA-DNA docking

Due to the difficulty of obtaining a DNA-bound crystal of HicBA, *in silico* molecular docking using the High Ambiguity Driven protein–protein DOCKing algorithm (HADDOCK) (60) was performed to examine the interaction between the promoter DNA and HicBA. The coordinates for a 28-base pair promoter DNA were modeled using the 3D-DART server (61), and the coordinates for HicBA were obtained from our crystal structure. The hetero-octamer model of the HicBA and the tetramer model of HicB were obtained by symmetry using the HicBA hetero-tetramer structure (PDB code 5YRZ). The residues of the DNA-binding domain inferred from the CSP values (Ile114–Thr117 in β1 for DNA recognition and Asn134–Gln137 in the N-terminal region of α2 for DNA anchoring and facing) and two symmetrical grooves of the DNA were defined as 'active residues' for the generation of the interface contact. Passive residues were defined automatically as the residues around the active residues.

In vitro ribonuclease assay after the addition of a peptide mimicking the binding region

The ribonuclease activity of HicA was confirmed using an RNase Alert Kit (IDT). A fluorescence quenching assay was performed according to the manufacturer's protocol. In this system, a fluorophore is covalently attached to one end of a synthetic RNA strand and is quenched by a quencher group at the other end. If synthetic RNA containing a fluorophore–quencher pair interacts with a ribonuclease, the synthetic RNA is digested, and the quencher is released. The released fluorophore emits fluorescence at 520 nm upon excitation at 490 nm. The resulting fluorescence (RFU) was observed on a SPECTRAmax GEMINI XS spectrofluorometer. The concentration range of HicA was varied to determine the ribonuclease activity of HicA and its reaction limits. HicA-H36A was examined by the same method as HicA to show the indispensability of His36 for the ribonuclease activity. Several short peptides that mimic the binding region of HicA were designed and purchased from ANYGEN (http://www.anygen.com). Peptides were added to the HicBA complex to release free HicA (Supplementary Table S3). The sequence of the peptide used in the regular experiment was 'ELNKYTERGIRKQAG'. Theoretically, mimicking peptides compete with the original protein for binding, if the peptide occupies the specific binding site, the toxin is released, producing fluorescence in the fluorescence quenching assay (62). The proteins and peptides used in ribonuclease assay were prepared in 20 mM Tris, pH 7.5 and 150 mM NaCl. The HicBA complex was incubated with the peptide for 30 min at 37°C before measurement of fluorescence.

In vivo cell growth assay

For the cell growth assay, the plasmids expressing HicBA, HicA and HicA-H36A were transformed into *E. coli* strain BL21(DE3). Transformed cells from single colonies grown on 0.1% glucose-containing M9 medium plates were grown overnight, and the overnight cultures were diluted to an OD_{600} of 0.1. The diluted cells were further grown until the OD_{600} of the cell suspension reached 0.4, at which time 0.5 mM IPTG was added to induce protein expression. The cells were incubated at 37°C for 8 h after induction by IPTG and monitored at 1-h intervals.

In vivo HicB neutralization assay

To assay neutralization by HicB, a mutational analysis of the binding interface of HicBA was conducted. Six residues of HicB (Phe22, Thr33, Gln34, Glu47, Phe80 and Thr89) were individually mutated to alanine (Supplementary Table S1A). The resulting mutant proteins were designated F22A, T33A, Q34A, E47A, F80A and T89A, respectively. The mutations were obtained by the same method used to prepare HicA-H36A, and the mutated HicBA complexes were expressed using the same procedures as those used for the native HicBA complex. The primers used to create these mutations are listed in Supplementary Table S1A. pET28b-HicA and pET21a-HicB, and pET28b-HicA and pET21a-HicB mutants were co-transformed into *E. coli* strain BL21 (DE3), respectively. The transformed cells were grown on LB plates containing 0.5 mM IPTG. The plates were incubated at 37°C for 18 h.

Circular dichroism (CD) spectroscopy

CD measurement of peptides dissolved in 20 mM Tris, pH 7.5 and 150 mM NaCl at a concentration of 25 μM was performed in a Chirascan Plus spectropolarimeter (Applied Photophysics, Ltd.) at 20°C using a cell with a 1 mm light path. CD scans were taken from 260 to 190 nm at bandwidth of 1 nm and a scan speed of 100 nm/min. The results of three scans were averaged, and the solvent signal was subtracted.

Antimicrobial activity test

The antimicrobial activity of the mimicking peptides was evaluated by measuring their minimum inhibitory concentration (MIC) values using the serial dilution method. The activity of the peptides against three strains of gram-positive (*Bacillus subtilis* ATCC 6633, *Staphylococcus aureus* ATCC 6538p, and *Staphylococcus epidermis* ATCC 12228) and five strains of gram-negative (*E. coli* ATCC 25922, *Shigella dysenteriae* ATCC 9752, *Salmonella typhimurium* ATCC 14028, *Klebsiella pneumoniae* ATCC 10031, and *Pseudomonas aeruginosa* ATCC 27853) bacteria was tested. Each bacterial strain was grown overnight in the presence of various concentrations of peptide (0.4–100 μM). The MIC was defined as the lowest peptide concentration that completely inhibited bacterial growth. Each test was conducted in duplicate.

RESULTS

Overall structure of the HicBA complex

The asymmetric unit of the HicBA complex crystal structure contains two hetero-dimeric HicBA complexes. Two HicB antitoxins and two HicA toxins form a hetero-tetrameric assembly (Figure 1A). However, the molecular weight of HicBA calculated from size-exclusion chromatography coupled with multi-angle light scattering (SEC-MALS) was 105 ± 0.1 kDa, which corresponds to the theoretical molecular weight of the hetero-octameric model of HicBA (105.4 kDa) (Supplementary Figure S1A). The model of the hetero-octameric assembly of HicBA contains dimeric interfaces between the HicB chains (Figure 1A and Supplementary Figure S2A). Secondary structure analysis was performed using the 2Struc server (63).

The *S. pneumoniae* HicB antitoxin contains three α-helices, three 3_{10}-helices (η) and four β-strands and the *S. pneumoniae* HicA toxin contains two α-helices and three β-strands with an α-β-β-β-α double-stranded RNA binding domain fold topology (Figure 1B). Compared to the structure of the *Y. pestis* HicBA complex (39), the structure of the *S. pneumoniae* HicBA complex contains an additional long, flexible loop between η1 and η2 of HicB (Supplementary Figure S2D). This loop is made up of more than 20 residues of HicB (Figure 1B). In particular, the C-terminal region of HicB, which is expected to be a DNA-binding domain, is not present in the structure of the *Y. pestis* HicBA complex (42) (Figure 1C). The structural topologies of the two HicBA complexes are described in Supplementary Figure S3A and B. The DNA-binding domain of the type II antitoxin is important in the auto-regulation of the TA operon (41). Furthermore, the DNA-binding domain of the HicBA system can form either a ribbon–helix–helix (43) or a helix-turn-helix (44). In summary, the structure of the *S. pneumoniae* HicBA complex presented here is the first to show the complete conformation of the HicBA TA system and can illuminate the biological function of the HicBA system.

The structural characteristics of HicB antitoxin

Two HicB antitoxins form a homodimer through their N-terminal domains, mainly β1, α1 and β4 of each HicB monomer. However, the molecular weight of HicB calculated from SEC-MALS was 71.8 ± 0.8 kDa, which corresponds to the theoretical molecular weight of a HicB tetramer (71.3 kDa) (Supplementary Figure S1B). The model of the HicB tetramer contains an additional C-terminal dimeric interface and an N-terminal interface. (Supplementary Figure S2B and C). The average area of the N-terminal dimeric interfaces is 602 $Å^2$. The interface area was calculated using the PISA server (64). The binding is achieved through both hydrophobic interactions and hydrogen bonding networks (Figure 2A).

Interestingly, considerable structural deviation is observed in the C-terminal domains of chains A and C of the two HicB antitoxins. The HicB antitoxin consists of an N-domain (residues 3–106), a hinge (residues 107–112), and a C-domain (residues 113–145). The rotation angle of the two C-domains of chains A and C is 151.3°. The root mean square deviation (r.m.s. deviation) value for the two N-domains is 0.81 Å, however, due to the flexibility of the C-domains, the r.m.s. deviation for the whole proteins is 10.63 Å. The N-domain, hinge and C-domains, the rotation angle, and the r.m.s deviation values were obtained using the *DynDom* database (65) (Figure 2B). Notably, the regions of the expected DNA-binding domain and the flexible C-domain are matched, indicating that the flexible nature of these domains is crucial to their role in DNA binding.

Characterization of the interaction of HicB and HicBA with promoter DNA

To confirm the DNA-binding properties of HicB and HicBA, an electrophoretic mobility shift assay (EMSA) experiment was conducted. Although we were not able to obtain the dissociation constant from the EMSA experiment, the binding properties of HicB and HicBA were determined based on the results. The concentration of DNA was fixed at 0.01 mM, and the concentration of the proteins was varied from 0 to 0.8 mM (HicB monomer and HicBA heterodimer). As the DNA bound to increasing amounts of protein, the bands corresponding to the DNA-protein complex shifted upward. (Figure 3A). EMSA showed that DNA binds to both the HicB antitoxin and the HicBA complex, exhibiting slightly higher affinity for HicBA than for HicB. However, no band shifts were observed in the case of the other palindromic sequences or the control 'X' DNA (Supplementary Figure S3C).

Isothermal titration calorimetry (ITC) experiments were used to estimate the affinity of binding of HicB and HicBA

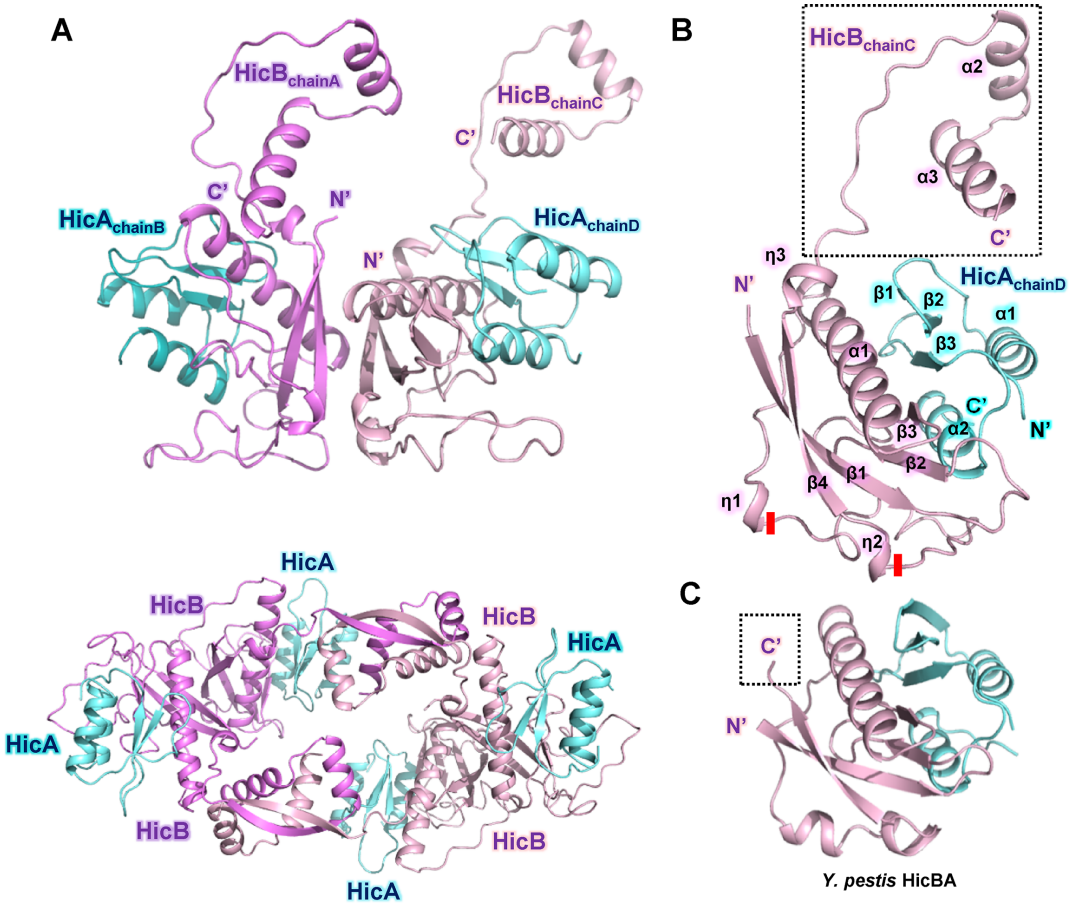

Figure 1. Overall structure of HicBA. (**A**) Upper: ribbon representation of the HicBA hetero-tetramer. Chains A and C of HicB are shown in purple, and chains B and D of HicA are shown in cyan. Lower: model of the HicBA hetero-octamer showing the dimeric interfaces between HicBs. (**B**) Structure of the HicBA heterodimer. The beginning and end of the long, flexible loop between η1 and η2 of HicB are marked by red bars. (**C**) Structure of the *Y. pestis* HicBA complex. (B and C) The entire DNA-binding domain of C-terminus of HicB is observed only in the structure of the *S. pneumoniae* HicBA complex, shown in the black dotted square. The structure of the *Y. pestis* HicBA complex lacks the C-terminal region of HicB.

to the promoter DNA (Figure 3B). The promoter DNA-binding reaction of HicB is endothermic and entropically driven, with thermodynamic parameters of 4.3 ± 0.4 kcal mol^{-1} ($\triangle H$) and 33.3 cal mol^{-1} deg^{-1} ($\triangle S$). The measured equilibrium dissociation constant (K_d) for the binding of HicB to DNA was 8.8 ± 1.1 μM. The binding stoichiometry (n) is 0.51 ± 0.02, indicating that one HicB dimer binds to each DNA duplex. The experimental values showed that the HicB tetramer interacts with dsDNA. The promoter DNA-binding reaction of HicBA is endothermic and entropically driven, with thermodynamic parameters of 6.5 ± 0.5 kcal mol^{-1} ($\triangle H$) and 44.6 cal mol^{-1} deg^{-1} ($\triangle S$), and the equilibrium dissociation constant (K_d) for the binding of HicBA to DNA was measured as 4.2 ± 0.4 μM. The binding stoichiometry (n) is 0.47 ± 0.03, indicating binding of one HicBA hetero-tetramer per DNA duplex. The experimental results showed that the HicBA hetero-octamer interacts with dsDNA and that, the HicBA complex has a higher affinity for DNA than HicB based on the K_d values. Calorimetric trials were also performed in the absence of proteins under the same experimental conditions. No changes in heat were observed in the control experiments.

DNA-binding domain of HicB

In type II TA systems, the antitoxin alone or in complex with the toxin typically interacts with its corresponding promoter DNA, repressing transcription from the TA operon (41). Therefore, the DNA-binding properties of the antitoxin are important for the regulation of TA systems. We characterized the interactions between specific residues in HicB and the promoter DNA using NMR titration experiments. In these experiments, HicB$^{109–150}$ was used because of the poor spectral quality of full-length HicB (Supplementary Figure S4A).

We predicted the possible DNA-binding domain of HicB and performed backbone assignment of HicB$^{109–150}$ with the exception of the residues Pro113 and Pro121. The secondary structure of HicB$^{109–150}$ in solution was derived from the program TALOS+ (66) using the assigned chemical shift values (Supplementary Table S4). The predicted conformation of HicB$^{109–150}$ includes one β-strand and two α-helices in the following order: β1 (residues 114–119), α1 (residues 122–130), and α2 (residues 135–145). The assigned β1–α1–α2 folding of the C-terminus of HicB corresponds to a ribbon-helix-helix motif (44). This conformation is highly consistent with the structure of HicB in the HicBA com-

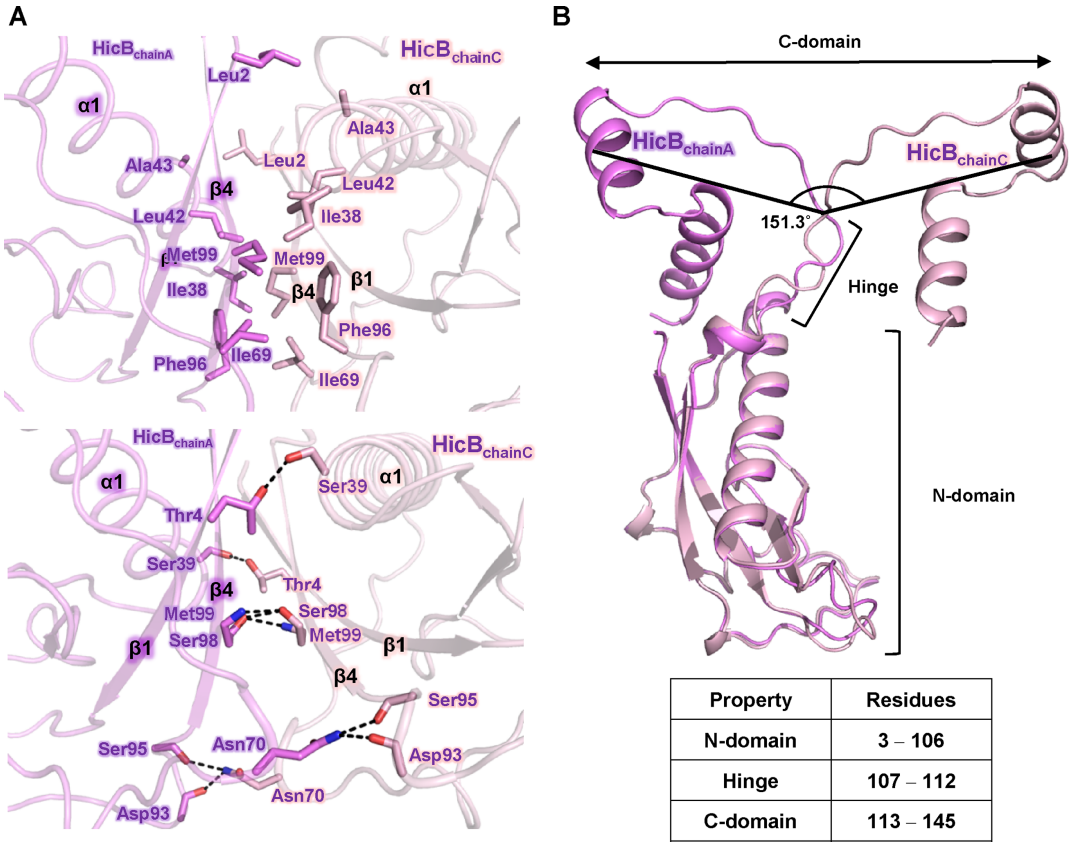

Property	Residues
N-domain	3 – 106
Hinge	107 – 112
C-domain	113 – 145

Figure 2. Structural features of the HicB dimer. (**A**) Details of the homodimeric interface between chains A and C of the HicB antitoxin. Upper: the residues involved in hydrophobic interactions. Residues participating in hydrophobic interactions are shown as stick models. Lower: the residues involved in hydrophilic interactions. Hydrogen bonds are shown as black dotted lines. (**B**) Structural deviation in the C' terminal domain of the two HicB antitoxins. The N-domains, hinge and C-domains and the rotation angle are indicated.

plex. Additionally, the DNA-binding domain of HicBA was superposed with the structures of other ribbon-helix-helix proteins that display DNA-binding affinity (Supplementary Figure S5A). The superposition is consistent with the idea that the DNA-binding domain consists of ribbon-helix-helix motif.

We compared the HSQC spectra of $HicB^{109–150}$ (1 mM, monomer concentration) in the absence and presence of increasing concentrations of promoter DNA (0–0.3 mM). These spectra are shown as an overlay in Figure 4A. Upon titration with DNA, the spectrum of $HicB^{109–150}$ showed a peak shift indicating that $HicB^{109–150}$–DNA interaction is achieved with fast exchange on the NMR time scale; such rapid exchange is typically observed when molecules bind with low to moderate affinity. The results of the titration experiment were consistent with the ITC data. According to the K_d determined in the ITC experiment, the binding of HicB to DNA is not strong; thus, binding between $HicB^{109–150}$ and DNA is expected to show rapid exchange. This result is highly consistent with the observed peak movements in the spectra of $HicB^{109–150}$ titrated with DNA. Additionally, as a result of additional titration, K_d for the binding of $HicBA^{109–150}$ to DNA was measured as 4.5 ± 1.1 μM; this is comparable to the K_d value calculated from ITC (Supplementary Figure S4B).

Based on the assigned backbone ^{1}H and ^{15}N resonances, we monitored the residues that showed changes in their chemical shifts upon binding of the protein to DNA. We calculated the combined ^{1}H and ^{15}N CSP values of $HicB^{109–150}$ in the presence of 0.3 mM DNA using Equation (1), (shown in the Materials and Methods section) to quantify the peak shifts. These values are plotted as a function of the $HicB^{109–150}$ residues (Figure 4B). The residues on the α2 helix and the C-terminus showed high CSP values. In particular, Phe135 and Gln137 on the N-terminus of the α2 helix and Val148 and Gln149 on the C-terminus exhibited significant changes in their chemical shifts. The residues in the β1 strand showed smaller CSP values than other secondary structure components because the hydrogen bonds between the β strands of the HicB dimer hinder large conformational changes (67). Based on these data, we characterized the DNA-binding region of $HicB^{109–150}$. The regions showing relatively large CSP values are mapped onto the surface representation of $HicB^{109–150}$ in Figure 4C. The darker-colored region in the generated surface is the region that is most affected during interaction with DNA.

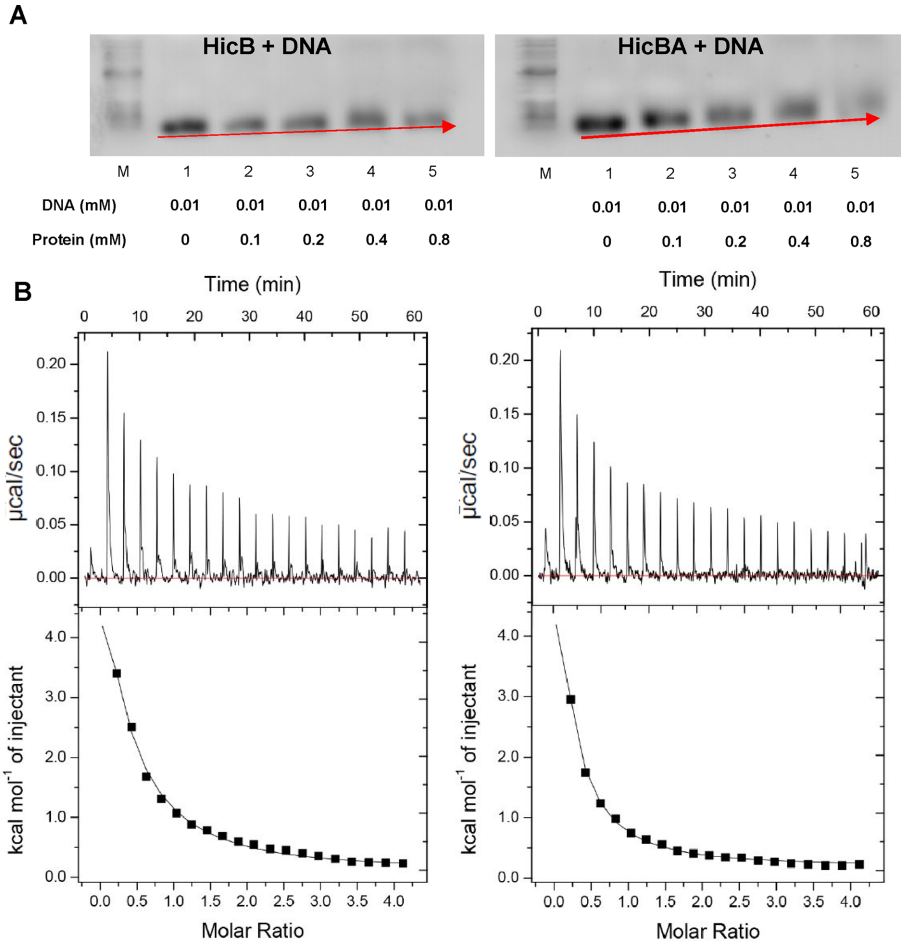

	n (The binding stoichiometry)	K_d (μM)	$\triangle H$ (kcal mol^{-1})	$T\triangle S$ (kcal mol^{-1})	$\triangle G$ (kcal mol^{-1})
HicB dimer	0.51 ± 0.02	8.8 ± 1.1	4.3 ± 0.4	9.92	-5.62
HicBA hetero-tetramer	0.47 ± 0.03	4.2± 0.4	6.5 ± 0.5	13.3	-6.76

Figure 3. Determination of the DNA-binding properties of HicB and HicBA using EMSA and ITC assays. (**A**) Left: EMSA experiment measuring the interaction between HicB and DNA. Right: EMSA experiment measuring the interaction between HicBA and DNA. The protein and DNA concentrations in each sample are indicated. The red arrows indicate the gradual formation of the DNA-protein complex at various protein:DNA ratios. As DNA binds gradually to larger amounts of the protein, the band representing the DNA-protein complex moves upward. (**B**) ITC assay of HicB (left) and HicBA (right) binding to promoter DNA. The titration binding curve indicates that HicB and HicBA are capable of binding to the upstream promoter DNA. The binding parameters are described in the table (lower).

The active site of HicA and its ribonuclease activity are dependent on His36

Type II toxins usually show ribonuclease activity, and certain essential residues are required for the organization of the active sites in the VapBC, RelBE, MazEF and PezAT systems (68). To identify the active site of the HicBA system, sequence alignment was performed using Clustal Omega 1.2.1 (69) and visualized using ESPript 3.0 (70) (Figure 5A). The sequence of *S. pneumoniae* HicA was aligned with the hypothetical protein from *Thermus thermophilus*, the HicA toxin from *Y. pestis*, the HicA toxin from *Burkholderia pseudomallei*, and the HicA toxin from *E. coli*. The results show a highly conserved histidine residue in the β2 strand and a conserved glycine residue in the loop between β1 and β2, corresponding to a hydrogen-bonded turn. For a detailed comparison, the structural similarity of these proteins was analyzed using DALI (71), with the exception of *E. coli* HicA, for which no structure has yet been reported.

The structural homologs include (i) the hypothetical protein from *T. thermophilus* [PDB code 1WHZ (chain A) with an r.m.s. deviation of 1.5 Å, a *Z*-score of 9.0 and a sequence identity of 29%], (ii) the HicA toxin from *Y. pestis* (39) [PDB code 4P78 (chains C and D) with r.m.s. deviations of 1.6–1.7 Å, *Z*-scores of 7.7–8.6 and a sequence identity of 34%]; and (iii) the HicA toxin from *B. pseudomallei* (47) [PDB code 4C26 (chain A) with an r.m.s. deviation of 2.3 Å, a *Z*-score of 5.7 and a sequence identity of 28%] (Supplementary Figure S5B).

In the active site of *S. pneumoniae* HicA, the key residue His36 interacts closely with Thr33 and Glu47 of the HicB

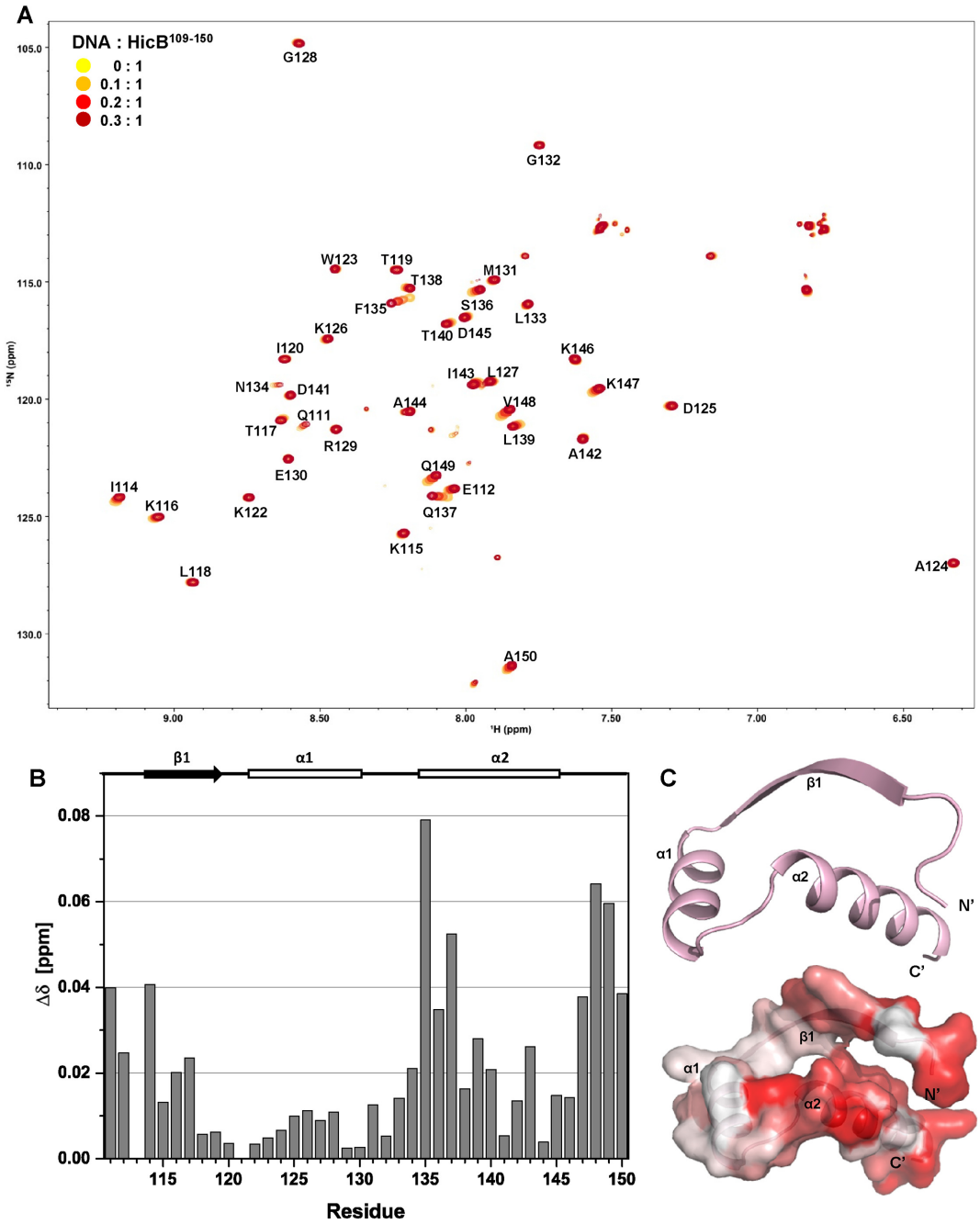

Figure 4. NMR titration of HicB$^{109–150}$ and its promoter DNA. (**A**) Overlay of the 2D ^{1}H-^{15}N HSQC spectra of 1 mM HicB$^{109–150}$ monomer in the presence of increasing ratios of added DNA. The peaks are colored with a gradient indicating the addition of DNA. (**B**) The CSP of each residue in the presence of 0.3 mM promoter DNA. (**C**) Upper: structure of HicB$^{109–150}$ in the HicBA complex. Lower: surface representation of HicB$^{109–150}$ with mapped CSP values. The residues are colored with a gradient indicating their CSP values.

antitoxin. The Oη_1 atom of Thr33 and the Oε_1 atom of Glu47 form hydrogen bonds with the Nε_2 atom and the N atom of this key residue. In addition, the Oε_1 atom of Glu47 greatly stabilizes the active site by forming a salt bridge with the Nδ_1 atom of the key residue. An intra-protein hydrogen bond between the N atom of the key residue His36 and the O atom of Lys33 in HicA is also observed (Figure 5B).

S. pneumoniae HicA forms a double-stranded RNA-binding domain (45). In the structure of the RNA-bound double-stranded RNA-binding domain (PDB code 1DI2) (72), α1 interacts with the minor groove of the RNA, and α2 interacts with the major groove of the RNA (Supplementary Figure S5C). RNA binding is mainly facilitated by these two α-helices; the β-strands make an insignificant contribution to RNA binding (73). HicA not only binds to RNA substrates but also cleaves them, thereby acting as a ribonuclease toxin (46). We assayed the RNase activity of HicA using fluorescent RNA substrates. When these sub-

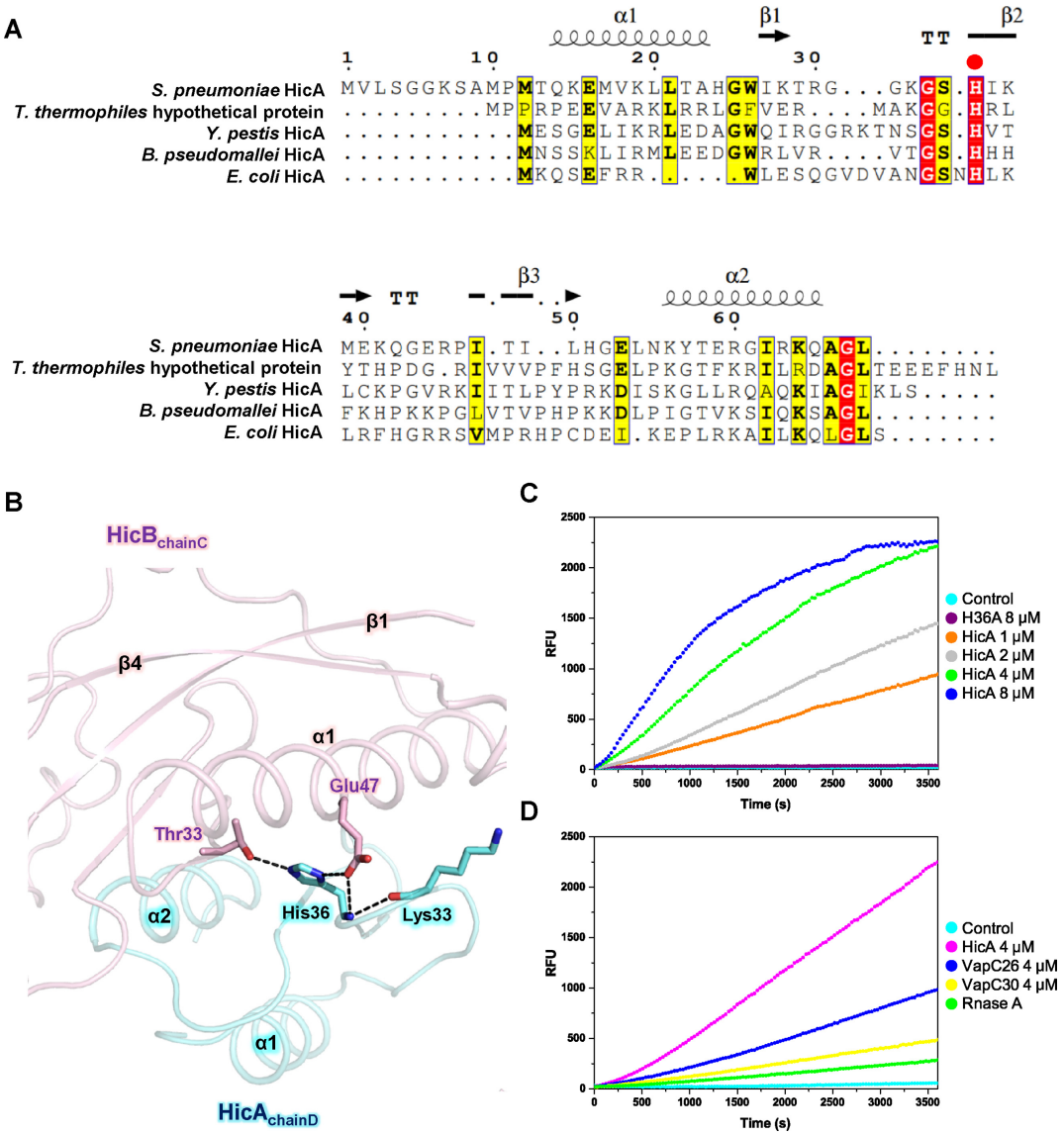

Figure 5. Sequence alignment of *S. pneumoniae* HicA showing sequence homologs, the active site structure of *S. pneumoniae* HicA, and the results of *in vitro* ribonuclease activity assays. (**A**) Proteins are listed in order of structural homology to *S. pneumoniae* HicA. The known secondary structural elements of the proteins are shown above the alignment. Identical and similar residues are highlighted in red and yellow, respectively. The conserved residue that is essential for ribonuclease activity, is indicated by a red circle. (**B**) Active site with nearby interacting residues. Hydrogen bonds and salt bridge are shown as black dotted lines. (**C**) Upper: fluorescence measurements as a function of time during addition of increasing amounts of HicA. Various concentrations of HicA monomer were prepared; at concentrations greater than 8 μM, the reaction was saturated. The protein with histidine mutated to alanine (H36A) showed negligible cleavage of the RNA molecule compared with HicA. (**D**) Comparison of the ribonuclease activity of *S. pneumoniae* HicA with that of other toxin molecules and RNase A. (C and D) Forty units of RiboLock™ (Thermo Scientific) RNase inhibitor were used to prevent ribonuclease contamination. The control contained 20 mM Tris, pH 7.5, 150 mM NaCl, and 40 units of RiboLock™ (Thermo Scientific) RNase inhibitor. Each experiment was performed in triplicate. In addition, 3×10^{-5} units of RNase A were used for comparison.

strates are cleaved, they emit fluorescence in proportion to the amount of the substrate cleaved. The ribonuclease activity of *S. pneumoniae* HicA was confirmed by the increase in the resulting fluorescence (RFU) as a function of the increase in the concentration of the HicA monomer protein from 1 μM to 8 μM (Figure 5C). At concentrations greater than 8 μM, the reaction was saturated. Due to loss of the key residue, HicA-H36A shows no ribonuclease activity. Compared to other toxin molecules with ribonuclease activity (VapC26 and VapC30 from *M. tuberculosis*), HicA showed the highest activity (Figure 5D).

Intermolecular interactions between HicB and HicA related to toxicity

The HicB antitoxin blocks the enzymatic function of the HicA toxin by forming the TA protein complex. In the toxin-neutralizing complex, HicB covers 1,183 Å^2 of HicA. Approximately 43% of the residues of HicA toxin chain D participate in this interaction, and the interface area occupies approximately 28% of the total surface area of HicA.

In the area of the interface, hydrophobic interactions are contributed by Phe22, Met44, Phe80, Phe86 and Tyr90 of

HicB and by Leu50 and Tyr57 of HicA. The aromatic interactions of Tyr57 of HicA are important in these hydrophobic interaction (Figure 6A). The HicB residues involved in hydrophilic interactions are Asp12, Ala19, Tyr30, Thr33, Gln34, Glu47, Thr89, Glu106 and Gln111; these residues interact with Arg30, Lys33, Ser35, His36, Lys38, Glu53, Asn55, Lys56, Tyr57, Thr58 and Gln65 of HicB. Additional salt bridges are formed by Asp12, Glu47, Asp55, and Asp83 of HicB and His36, Lys38, Lys56 and Lys64 of HicA (Figure 6B). The overall hydrophilic networks are presented in a schematic diagram.

To verify the key residues that are essential for the interaction between HicB and HicA, six residues of HicB were mutated to alanine based on the interaction analysis shown in Figure 6A and B. Four residues involved in hydrophilic interactions with multiple counterparts in HicA (Thr33, Gln34, Glu47 and Thr89) and two other residues involved in hydrophobic interactions (Phe22 and Phe80) were selected. Complexes of HicA with HicB-F22A and HicB-E47A resulted in decreased growth of *E. coli*, suggesting that mutation of Phe22 or Glu47 resulted in loss of the interaction between HicB and HicA. *E. coli* cells containing HicA-HicB-F22A and HicA-HicB-E47A produced far fewer colonies than *E. coli* cells containing the native HicBA complex (Figure 6C).

Artificial toxin activation and inhibition of cell growth by HicA

We designed peptides that mimic the binding interface of HicA to inhibit the interaction between HicB and HicA. Theoretically, these mimicking peptides should compete with HicA and hinder the formation of the TA complex. If a peptide displays high affinity for HicB, more free HicA will be present, resulting in increased RNase activity (62). The data presented in the main figure were obtained from experiments using the peptide 'ELNKYTERGIRKQAG', the activity of which was compared with that of other candidate peptides (Supplementary Figure S6A and B). The chosen peptide contains 11 residues corresponding to the α2 helix region of HicA (KYTERGIRKQA) and 11 residues corresponding to the interface between HicA and HicB; these residues are underlined. Peptides mimicking the helix are preferred because of their resistance to proteolytic degradation (74). Due to its membrane affinity and selectivity, the modeled helix should not be divided. Additionally, the optimal length of the helix should be modeled to prevent loss of selectivity and self-aggregation (75). The circular dichroism spectra of the peptides were determined; the peptide 'ELNKYTERGIRKQAG' showed the highest degree of helicity (39.8%). The helical content of each peptide was quantitatively measured based on the mean residue ellipticity, $[\theta]_{222}$ (76) (Supplementary Figure S6C).

The designed mimicking peptide includes the entire α2 helix of HicA and contains seven residues (Glu53, Asn55, Lys56, Tyr57, Thr58, Lys64 and Gln65) that participate in interactions with HicB. The peptide disrupts the interaction of the HicBA complex by up to 80% (Figure 7A and B). The RFU at peptide concentrations greater than 16 μM did not show a marked difference from that observed at 16 μM.

Cell growth assays demonstrated the ability of HicA to arrest bacterial growth and the loss of toxicity of HicA-H36A (Figure 7C). *E. coli* cells expressing HicA showed decreased OD_{600} beginning at 2 h after induction. Cells expressing HicA-H36A grew at the same rate as the control cells.

The antimicrobial activity of the mimicking peptide is summarized in Figure 7D. The peptide exhibited detectable activities against certain bacterial species. The peptide with the strongest activity against both gram-positive and gram-negative bacteria had the smallest MIC value of 6.3 μM.

DISCUSSION

Structural uniqueness of the HicBA complex

The structure of HicBA of *S. pneumoniae* presented here is the first structure to show the complete conformation of the HicBA TA system. The mechanism of assembly of the HicBA complex involves two dimerization regions of HicB that are located in its N-terminus and its C-terminus. The interface of *Y. pestis* HicBA was studied earlier (39), but the structural and functional characteristics of the flexible DNA-binding domain of HicB are revealed by our study. NMR assignments confirmed that the C-terminal DNA-binding motif of HicB is a ribbon-helix-helix (43). The DNA-binding domain corresponds to the flexible C-domain; demonstration of the flexible nature of HicBA provides a supplementary explanation for many flexible-domain-lacking TA complexes (68,77). In addition, because an intrinsically disordered toxin-neutralizing domain modulates the affinity between the antitoxin and DNA, further study of the relationship between protein flexibility and disorder should yield crucial insights into the reversibility of TA action, including folding upon binding (78).

According to our SEC-MALS data, *S. pneumoniae* HicBA actually forms a hetero-octamer in solution. The radius of gyration (Rg) calculated from the hetero-octamer model by CRYSOL (79) (33.6 Å) was consistent with that obtained by analysis using SEC-MALS (35.7 Å). The hetero-tetramer model of HicBA in the crystal structure forms a very flexible and highly mobile structure in which there are no contacts between the C-terminal region of HicB and the remainder of the protein complex (Figure 1A). In addition, the functional unit of the ribbon-helix-helix motif is a dimer that contains a tight, stable antiparallel β-sheet (43). The functional unit of RHH is observed in the hetero-octamer model but not in the hetero-tetramer model (Figure 1A). Therefore, the observed conformation of the hetero-tetramer is probably biased by lattice contacts and may not correspond to its true solution structure. Furthermore, HicBs from both *S. pneumoniae* and *Y. pestis* form tetramers as shown by SEC-MALS data (39), which means that HicB requires homo-dimeric interfaces at both its N- and C-termini to form the tetramer (Supplementary Figure S2B). This experimental evidence is consistent with a hetero-octamer model of HicBA.

Insights into the DNA-binding mechanism of HicB

According to the structural analysis, HicB from *S. pneumoniae* is composed of three domains: an N-domain, a hinge

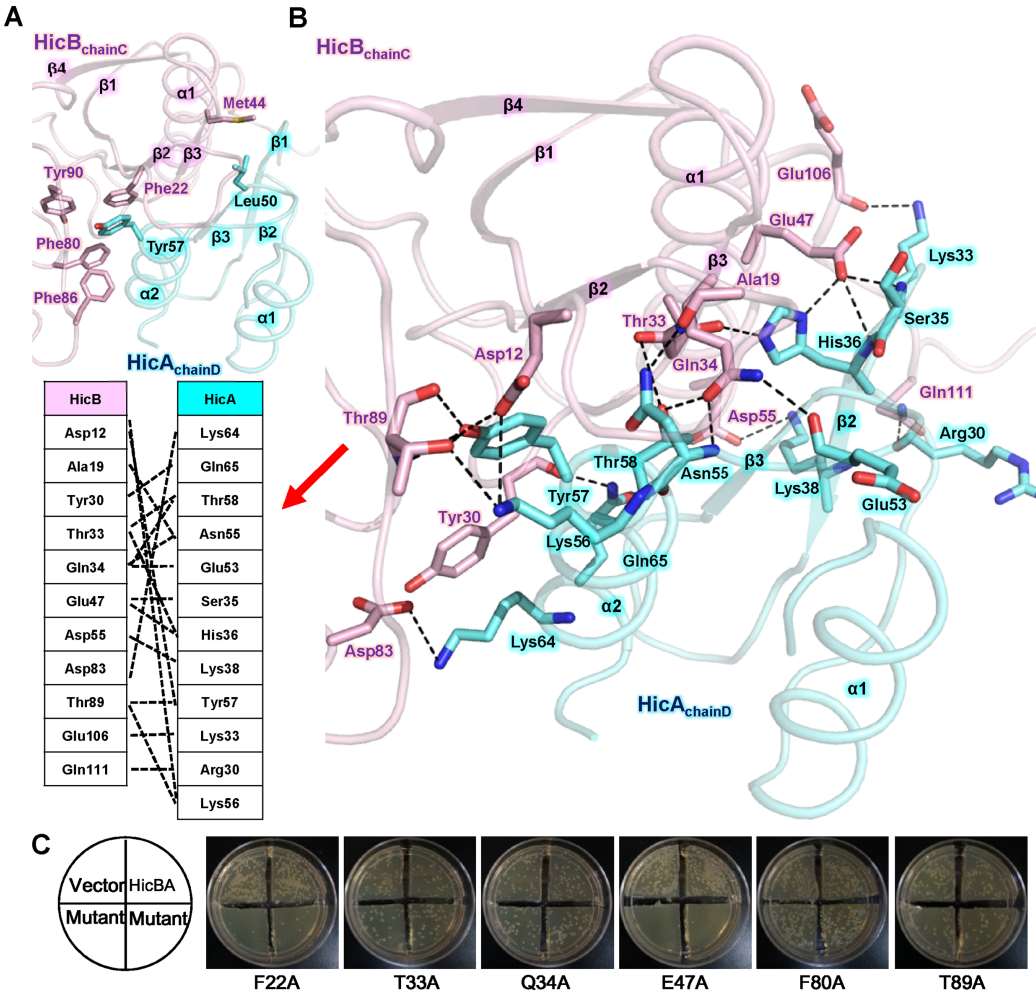

Figure 6. Heterodimeric interface of HicB and HicA showing the mutations that affect toxicity. (**A**) Range of hydrophobic forces mainly contributed by Tyr57 of HicA. (**B**) Residues involved in hydrophilic interactions. Hydrogen bonds and salt bridges are shown as black dotted lines. Schematic diagrams of the hydrophilic interactions indicated by red arrows in Figure 6B are presented. (**C**) Effect of the mutation of residues involved in the interaction between HicB and HicA on the growth of *E. coli* cells. Mutated complexes were induced by IPTG to determine the toxicity to *E. coli* cells. The upper two quadrants indicate the empty vectors and the native HicBA complex. The decreased number of colonies in the lower quadrants indicates that the activity of the mutated HicBA complex was regained.

and a C-domain. The hinge is flexible and is formed by residues 107–112. The flexibility of the substrate-binding region of the protein is significantly associated with the specificity of its substrate. Thus, the conformational flexibility of the binding site greatly influences the protein's DNA-binding specificity (80). Based on our study, the flexible nature of HicB plays a crucial role in the protein's regulatory dynamics with respect to its target DNA (81,82). As a transcriptional regulator, the flexible form of HicB is essential for bacterial cell life and death. The flexible domains of the protein undergo a folding transition upon binding to toxins or DNA and thereby exert important regulatory functions. In other words, the intrinsic flexibility of HicB confers functional advantages and enables HicB to bind to its target easily (83,84).

Stabilization of the conformation of protein upon binding to its substrate might also explain the greater binding affinity of HicBA-DNA than that of HicB-DNA. HicA contributes thermodynamically to the binding affinity and the structural stability of HicB and DNA (85,86). The mechanical process of binding of HicBA to DNA can be understood by analyzing their interaction at the atomic level (Supplementary Figure S7A and B). In our model, two antiparallel β-sheets bind to the major groove of DNA, and the electrostatically positive portions of the two α-helices anchor the DNA facing the phosphates of the DNA backbone. These binding characteristics of HicBA-DNA interactions are mediated by a stabilization-upon-binding mechanism that increases substrate specificity through conformational changes that occur upon the binding of the three binding partners HicB, HicA and DNA (87,88).

New interactions involved in the active site of HicA

The active sites of toxins belonging to the VapBC and RelBE families consist of three to four conserved residues and possible additional residues (89,90). The residues comprising the active site are counteracted by binding of the cognate antitoxins. In proteins of the HicBA family, how-

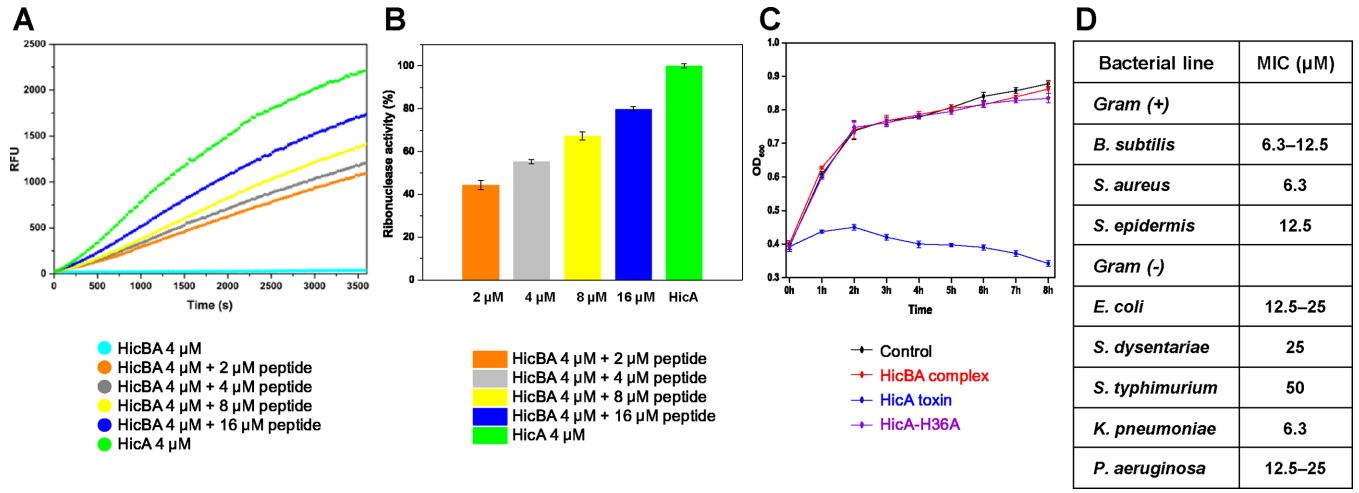

D

Bacterial line	MIC (μM)
Gram (+)	
B. subtilis	6.3–12.5
S. aureus	6.3
S. epidermis	12.5
Gram (-)	
E. coli	12.5–25
S. dysentariae	25
S. typhimurium	50
K. pneumoniae	6.3
P. aeruginosa	12.5–25

Figure 7. Measurement of the ribonuclease activity of *S. pneumoniae* HicBA using a HicA α2-mimicking peptide and cell growth inhibition activity of the HicA toxin and the mimicking peptide. (**A**) The concentration of HicBA hetero-dimer was fixed at 4 μM, and the concentration of the peptide was increased from 2 to 16 μM. The peptide inhibited the binding of HicB to HicA by approximately 80% at 16 μM. Forty units of RiboLock^{TM} (Thermo Scientific) RNase inhibitor were used to prevent ribonuclease contamination. Each experiment was performed in triplicate. (**B**) Statistical representation of the data shown in (A). The RFU obtained with 4 μM HicA monomer was taken as 100%, and that obtained with 4 μM HicBA hetero-dimer was taken as 0%. The x-axis indicates the concentration of added peptide. The error bars indicate the standard deviations of the values obtained in three replicate reactions. (**C**) *In vivo* assay of HicA toxicity. Each cell growth curve is shown in a different color. The data (OD_{600}) show the average values obtained in triplicate reactions; the standard deviations are indicated by error bars. (**D**) Antimicrobial activity of the mimicking peptide against various bacteria. The MIC was defined as the lowest peptide concentration (μM) that completely inhibited cell growth after 24 h of incubation at 37°C. The experiment was performed in duplicate.

ever, only one conserved histidine is present in the reported HicA toxins, and this histidine residue is likely to contribute to the toxicity of the protein (Figure 5B). Our mutation experiments confirmed that His36 is a critical source of toxin activity (Figure 5C). Furthermore, HicA toxins are smaller than MazF, RelE and VapC, and their active sites do not include any charged pockets, clusters or cavities (48,91,92) (Supplementary Figure S8). The presence of a conserved glycine and serine near His36 might support the structural integrity of the active site.

In contrast, interesting structural discoveries illuminate the mechanism of blocking of the active site in *Y. pestis* (39) and *S. pneumoniae* HicBA. In *S. pneumoniae* HicBA, His36 of HicA protrudes but is blocked by Thr33 and Glu47 of HicB. As a result of this interaction, these three residues form a catalytic triad (93) (Supplementary Figure S9). The catalytic triad consists of an acid, a base and a nucleophile. A similar triad is found in *Y. pestis* HicBA. The amino acids acting as the acid and base are the same in the two structures, a glutamate and a histidine, but the residue acting as a nucleophile is a threonine in *S. pneumoniae* and an asparagine in *Y. pestis* (94). A catalytic triad is usually located within the active site of a protease (95), but the type II toxin HicA is a ribonuclease and requires His36 for its ribonuclease activity. Therefore, the ribonuclease activity of HicA can be rationally suggested to be inhibited by a folding triad that cannot cut RNA and that is formed via binding to HicB. This explanation is consistent with the results of the mutational study obtained in the HicB neutralization assay, which showed that HicA-HicB-E47A (the HicBA complex with the E47A mutation in HicB) resulted in regeneration of the toxicity of HicA to cells (Figure 6C). The role of the acid is estimated to be more important than that of the variable nucleophiles because HicA-HicB-T33A did not show toxicity to cells.

Artificial activation of HicA by a mimicking peptide as an antibacterial strategy

Based on the toxicity of HicA shown in our study (Figure 7C), our peptide inhibitors can act as a novel antimicrobial agent by liberating HicA from the HicBA complex. Peptides that mimic the HicBA complex have greater ability to inhibit the interaction between toxin and antitoxin independent of the concentration of peptide than other TA-complex-mimicking peptides (48,49,96). Furthermore, the MIC of the tested peptides could be obtained via an antimicrobial activity test, despite its relatively high value compared with that of other highly engineered antimicrobial peptides (74,97). The fact that the antimicrobial activity of peptides with higher α-helical content and better folding was greater (Supplementary Figure S6C) suggests that we might be able to obtain a more optimized inhibitor by modifying the peptide using conjugation strategies and surface modulation such as stapling the peptides via hydrocarbon cross-linking to obtain better permeability and structural folding (98,99).

The expression of HicA protein in *E. coli* has been shown to severely reduce the translation rate (100), and the expression of HicA in *B. pseudomallei* was associated with modulation of the formation of persister cells (47). The inhibitory peptides designed for use in this study are based on the structure of the TA interface. Therefore, it is possible that these inhibitory peptides could bind to and inhibit the TA complexes of other bacteria that show structural similarity to HicBA. In conclusion, based on the experimental data obtained in this study, a peptide inducing adequate activa-

tion of HicA may serve as a new structure-based antimicrobial agent.

DATA AVAILABILITY

The structure described in this work has been deposited in the Protein Data Bank (PDB) under the accession code 5YRZ.

SUPPLEMENTARY DATA

Supplementary Data are available at NAR Online.

ACKNOWLEDGEMENTS

We thank the beamline staff at Pohang Light Source, Korea (BL-5C and 7A) and SPring-8, Japan (BL44XU).

FUNDING

National Research Foundation of Korea (NRF) through a grant funded by the Korean government (MEST) [2018R1A2A1A19018526, 2018R1A5A2024425]; 2017 BK21 Plus Project for Medicine, Dentistry and Pharmacy. Funding for open access charge: National Research Foundation of Korea.
Conflict of interest statement. None declared.

REFERENCES

1. Jacobs,M.R. (2004) Streptococcus pneumoniae: epidemiology and patterns of resistance. *Am. J. Med.*, **117**(Suppl. 3A), 3S–15S.
2. Kaplan,S.L. (1995) The emergence of resistant pneumococcus as a pathogen in childhood upper respiratory tract infections. *Semin. Respir. Infect.*, **10**, 31–36.
3. Ge,M., Chen,Z., Onishi,H.R., Kohler,J., Silver,L.L., Kerns,R., Fukuzawa,S., Thompson,C. and Kahne,D. (1999) Vancomycin derivatives that inhibit peptidoglycan biosynthesis without binding D-Ala-D-Ala. *Science*, **284**, 507–511.
4. Chambers,H.F. (1999) Penicillin-binding protein-mediated resistance in pneumococci and staphylococci. *J. Infect. Dis.*, **179**(Suppl. 2), S353–359.
5. Croucher,N.J., Chewapreecha,C., Hanage,W.P., Harris,S.R., McGee,L., van der Linden,M., Song,J.H., Ko,K.S., de Lencastre,H., Turner,C. *et al.* (2014) Evidence for soft selective sweeps in the evolution of pneumococcal multidrug resistance and vaccine escape. *Genome Biol. Evol.*, **6**, 1589–1602.
6. Dagan,R. (2009) Impact of pneumococcal conjugate vaccine on infections caused by antibiotic-resistant Streptococcus pneumoniae. *Clin. Microbiol. Infect.*, **15**(Suppl. 3), 16–20.
7. Rivera,A.M. and Boucher,H.W. (2011) Current concepts in antimicrobial therapy against select gram-positive organisms: methicillin-resistant Staphylococcus aureus, penicillin-resistant pneumococci, and vancomycin-resistant enterococci. *Mayo Clin. Proc.*, **86**, 1230–1243.
8. Fernandes,P. (2006) Antibacterial discovery and development–the failure of success? *Nat. Biotechnol.*, **24**, 1497–1503.
9. Spiegel,C.A. (1988) Laboratory detection of high-level aminoglycoside-aminocyclitol resistance in Enterococcus spp. *J. Clin. Microbiol.*, **26**, 2270–2274.
10. Bliziotis,I.A., Samonis,G., Vardakas,K.Z., Chrysanthopoulou,S. and Falagas,M.E. (2005) Effect of aminoglycoside and beta-lactam combination therapy versus beta-lactam monotherapy on the emergence of antimicrobial resistance: a meta-analysis of randomized, controlled trials. *Clin. Infect. Dis.*, **41**, 149–158.
11. Buts,L., Lah,J., Dao-Thi,M.H., Wyns,L. and Loris,R. (2005) toxin–antitoxin modules as bacterial metabolic stress managers. *Trends Biochem. Sci.*, **30**, 672–679.
12. Gerdes,K., Christensen,S.K. and Lobner-Olesen,A. (2005) Prokaryotic toxin–antitoxin stress response loci. *Nat. Rev. Microbiol.*, **3**, 371–382.
13. Van Melderen,L. (2010) toxin–antitoxin systems: why so many, what for? *Curr. Opin. Microbiol.*, **13**, 781–785.
14. Hayes,F. and Van Melderen,L. (2011) Toxins-antitoxins: diversity, evolution and function. *Crit. Rev. Biochem. Mol. Biol.*, **46**, 386–408.
15. Long,Q.X., He,Y. and Xie,J.P. (2012) [The molecular physiological and genetic mechanisms underlying the superb efficacy of quinolones]. *Yao Xue Xue Bao*, **47**, 969–977.
16. Ogura,T. and Hiraga,S. (1983) Mini-F plasmid genes that couple host cell division to plasmid proliferation. *Proc. Natl. Acad. Sci. U.S.A.*, **80**, 4784–4788.
17. Magnuson,R.D. (2007) Hypothetical functions of toxin–antitoxin systems. *J. Bacteriol.*, **189**, 6089–6092.
18. Monti,M.C., Hernandez-Arriaga,A.M., Kamphuis,M.B., Lopez-Villarejo,J., Heck,A.J., Boelens,R., Diaz-Orejas,R. and van den Heuvel,R.H. (2007) Interactions of Kid-Kis toxin–antitoxin complexes with the parD operator-promoter region of plasmid R1 are piloted by the Kis antitoxin and tuned by the stoichiometry of Kid-Kis oligomers. *Nucleic Acids Res.*, **35**, 1737–1749.
19. Wang,X. and Wood,T.K. (2011) toxin–antitoxin systems influence biofilm and persister cell formation and the general stress response. *Appl. Environ. Microbiol.*, **77**, 5577–5583.
20. Vazquez-Laslop,N., Lee,H. and Neyfakh,A.A. (2006) Increased persistence in Escherichia coli caused by controlled expression of toxins or other unrelated proteins. *J. Bacteriol.*, **188**, 3494–3497.
21. Korch,S.B. and Hill,T.M. (2006) Ectopic overexpression of wild-type and mutant hipA genes in Escherichia coli: effects on macromolecular synthesis and persister formation. *J. Bacteriol.*, **188**, 3826–3836.
22. Yamaguchi,Y., Park,J.H. and Inouye,M. (2011) toxin–antitoxin systems in bacteria and archaea. *Annu. Rev. Genet.*, **45**, 61–79.
23. Zhu,L., Zhang,Y., Teh,J.S., Zhang,J., Connell,N., Rubin,H. and Inouye,M. (2006) Characterization of mRNA interferases from Mycobacterium tuberculosis. *J. Biol. Chem.*, **281**, 18638–18643.
24. Dao-Thi,M.H., Van Melderen,L., De Genst,E., Afif,H., Buts,L., Wyns,L. and Loris,R. (2005) Molecular basis of gyrase poisoning by the addiction toxin CcdB. *J. Mol. Biol.*, **348**, 1091–1102.
25. Christensen,S.K. and Gerdes,K. (2003) RelE toxins from bacteria and Archaea cleave mRNAs on translating ribosomes, which are rescued by tmRNA. *Mol. Microbiol.*, **48**, 1389–1400.
26. Ramisetty,B.C. and Santhosh,R.S. (2016) Horizontal gene transfer of chromosomal Type II toxin–antitoxin systems of Escherichia coli. *FEMS Microbiol. Lett.*, **363**, fnv238.
27. Fiedoruk,K., Daniluk,T., Swiecicka,I., Sciepuk,M. and Leszczynska,K. (2015) Type II toxin–antitoxin systems are unevenly distributed among Escherichia coli phylogroups. *Microbiology*, **161**, 158–167.
28. Aakre,C.D., Phung,T.N., Huang,D. and Laub,M.T. (2013) A bacterial toxin inhibits DNA replication elongation through a direct interaction with the beta sliding clamp. *Mol. Cell*, **52**, 617–628.
29. Janssen,B.D., Garza-Sanchez,F. and Hayes,C.S. (2015) YoeB toxin is activated during thermal stress. *Microbiologyopen*, **4**, 682–697.
30. Kedzierska,B. and Hayes,F. (2016) Emerging roles of toxin–antitoxin modules in bacterial pathogenesis. *Molecules*, **21**, 790.
31. Schuster,C.F. and Bertram,R. (2016) Toxin–antitoxin systems of Staphylococcus aureus. *Toxins (Basel)*, **8**, 140.
32. Brzozowska,I. and Zielenkiewicz,U. (2013) Regulation of toxin–antitoxin systems by proteolysis. *Plasmid*, **70**, 33–41.
33. Nieto,C., Cherny,I., Khoo,S.K., de Lacoba,M.G., Chan,W.T., Yeo,C.C., Gazit,E. and Espinosa,M. (2007) The yefM-yoeB toxin–antitoxin systems of Escherichia coli and Streptococcus pneumoniae: functional and structural correlation. *J. Bacteriol.*, **189**, 1266–1278.
34. Chan,W.T., Balsa,D. and Espinosa,M. (2015) One cannot rule them all: are bacterial toxins-antitoxins druggable? *FEMS Microbiol. Rev.*, **39**, 522–540.
35. Shao,Y., Harrison,E.M., Bi,D., Tai,C., He,X., Ou,H.Y., Rajakumar,K. and Deng,Z. (2011) TADB: a web-based resource for Type 2 toxin–antitoxin loci in bacteria and archaea. *Nucleic Acids Res.*, **39**, D606–D611.

36. Ramage,H.R., Connolly,L.E. and Cox,J.S. (2009) Comprehensive functional analysis of Mycobacterium tuberculosis toxin–antitoxin systems: implications for pathogenesis, stress responses, and evolution. *PLoS Genet.*, **5**, e1000767.
37. Sala,A., Bordes,P. and Genevaux,P. (2014) Multiple toxin–antitoxin systems in Mycobacterium tuberculosis. *Toxins (Basel)*, **6**, 1002–1020.
38. Miallau,L., Faller,M., Chiang,J., Arbing,M., Guo,F., Cascio,D. and Eisenberg,D. (2009) Structure and proposed activity of a member of the VapBC family of toxin–antitoxin systems. VapBC-5 from Mycobacterium tuberculosis. *J. Biol. Chem.*, **284**, 276–283.
39. Bibi-Triki,S., Li de la Sierra-Gallay,I., Lazar,N., Leroy,A., Van Tilbeurgh,H., Sebbane,F. and Pradel,E. (2014) Functional and structural analysis of HicA3-HicB3, a novel toxin–antitoxin system of Yersinia pestis. *J. Bacteriol.*, **196**, 3712–3723.
40. Goeders,N. and Van Melderen,L. (2014) toxin–antitoxin systems as multilevel interaction systems. *Toxins (Basel)*, **6**, 304–324.
41. Bukowski,M., Rojowska,A. and Wladyka,B. (2011) Prokaryotic toxin–antitoxin systems–the role in bacterial physiology and application in molecular biology. *Acta Biochim. Pol.*, **58**, 1–9.
42. Makarova,K.S., Grishin,N.V. and Koonin,E.V. (2006) The HicAB cassette, a putative novel, RNA-targeting toxin–antitoxin system in archaea and bacteria. *Bioinformatics*, **22**, 2581–2584.
43. Schreiter,E.R. and Drennan,C.L. (2007) Ribbon-helix-helix transcription factors: variations on a theme. *Nat. Rev. Microbiol.*, **5**, 710–720.
44. Xiong,W., Li,T., Chen,K. and Tang,K. (2009) Local combinational variables: an approach used in DNA-binding helix-turn-helix motif prediction with sequence information. *Nucleic Acids Res.*, **37**, 5632–5640.
45. Masliah,G., Barraud,P. and Allain,F.H. (2013) RNA recognition by double-stranded RNA binding domains: a matter of shape and sequence. *Cell. Mol. Life Sci.*, **70**, 1875–1895.
46. Unterholzner,S.J., Poppenberger,B. and Rozhon,W. (2013) toxin–antitoxin systems: biology, identification, and application. *Mob. Genet. Elements*, **3**, e26219.
47. Butt,A., Higman,V.A., Williams,C., Crump,M.P., Hemsley,C.M., Harmer,N. and Titball,R.W. (2014) The HicA toxin from Burkholderia pseudomallei has a role in persister cell formation. *Biochem. J.*, **459**, 333–344.
48. Kang,S.M., Kim,D.H., Lee,K.Y., Park,S.J., Yoon,H.J., Lee,S.J., Im,H. and Lee,B.J. (2017) Functional details of the Mycobacterium tuberculosis VapBC26 toxin–antitoxin system based on a structural study: insights into unique binding and antibiotic peptides. *Nucleic Acids Res.*, **45**, 8564–8580.
49. Lee,I.G., Lee,S.J., Chae,S., Lee,K.Y., Kim,J.H. and Lee,B.J. (2015) Structural and functional studies of the Mycobacterium tuberculosis VapBC30 toxin–antitoxin system: implications for the design of novel antimicrobial peptides. *Nucleic Acids Res.*, **43**, 7624–7637.
50. Otwinowski,Z. and Minor,W. (1997) Processing of X-ray diffraction data collected in oscillation mode. *Macromol. Crystallogr. A*, **276**, 307–326.
51. Adams,P.D., Afonine,P.V., Bunkoczi,G., Chen,V.B., Davis,I.W., Echols,N., Headd,J.J., Hung,L.W., Kapral,G.J., Grosse-Kunstleve,R.W. *et al.* (2010) PHENIX: a comprehensive Python-based system for macromolecular structure solution. *Acta Crystallogr. D Biol. Crystallogr.*, **66**, 213–221.
52. Emsley,P., Lohkamp,B., Scott,W.G. and Cowtan,K. (2010) Features and development of Coot. *Acta Crystallogr. D Biol. Crystallogr.*, **66**, 486–501.
53. Brunger,A.T. (1992) Free R value: a novel statistical quantity for assessing the accuracy of crystal structures. *Nature*, **355**, 472–475.
54. Murshudov,G.N., Skubak,P., Lebedev,A.A., Pannu,N.S., Steiner,R.A., Nicholls,R.A., Winn,M.D., Long,F. and Vagin,A.A. (2011) REFMAC5 for the refinement of macromolecular crystal structures. *Acta Crystallogr. D Biol. Crystallogr.*, **67**, 355–367.
55. Chen,V.B., Arendall,W.B. 3rd, Headd,J.J., Keedy,D.A., Immormino,R.M., Kapral,G.J., Murray,L.W., Richardson,J.S. and Richardson,D.C. (2010) MolProbity: all-atom structure validation for macromolecular crystallography. *Acta Crystallogr. D Biol. Crystallogr.*, **66**, 12–21.
56. Delano,W.L. (2002) *The PyMOL Molecular Graphics System*. DeLano Scientific, San Carlos.
57. Baker,N.A., Sept,D., Joseph,S., Holst,M.J. and McCammon,J.A. (2001) Electrostatics of nanosystems: application to microtubules and the ribosome. *Proc. Natl. Acad. Sci. U.S.A.*, **98**, 10037–10041.
58. Delaglio,F., Grzesiek,S., Vuister,G.W., Zhu,G., Pfeifer,J. and Bax,A. (1995) NMRPipe: a multidimensional spectral processing system based on UNIX pipes. *J. Biomol. NMR*, **6**, 277–293.
59. Johnson,B.A. (2004) Using NMRView to visualize and analyze the NMR spectra of macromolecules. *Methods Mol. Biol.*, **278**, 313–352.
60. Dominguez,C., Boelens,R. and Bonvin,A.M. (2003) HADDOCK: a protein–protein docking approach based on biochemical or biophysical information. *J. Am. Chem. Soc.*, **125**, 1731–1737.
61. van Dijk,M. and Bonvin,A.M. (2009) 3D-DART: a DNA structure modelling server. *Nucleic Acids Res.*, **37**, W235–W239.
62. Verma,S., Kumar,S., Gupta,V.P., Gourinath,S., Bhatnagar,S. and Bhatnagar,R. (2015) Structural basis of Bacillus anthracis MoxXT disruption and the modulation of MoxT ribonuclease activity by rationally designed peptides. *J. Biomol. Struct. Dyn.*, **33**, 606–624.
63. Klose,D.P., Wallace,B.A. and Janes,R.W. (2010) 2Struc: the secondary structure server. *Bioinformatics*, **26**, 2624–2625.
64. Krissinel,E. and Henrick,K. (2007) Inference of macromolecular assemblies from crystalline state. *J. Mol. Biol.*, **372**, 774–797.
65. Lee,R.A., Razaz,M. and Hayward,S. (2003) The DynDom database of protein domain motions. *Bioinformatics*, **19**, 1290–1291.
66. Shen,Y., Delaglio,F., Cornilescu,G. and Bax,A. (2009) TALOS+: a hybrid method for predicting protein backbone torsion angles from NMR chemical shifts. *J. Biomol. NMR*, **44**, 213–223.
67. Kim,D.H., Kang,S.J., Lee,K.Y., Jang,S.B., Kang,S.M. and Lee,B.J. (2017) Structure and dynamics study of translation initiation factor 1 from Staphylococcus aureus suggests its RNA binding mode. *Biochim. Biophys. Acta*, **1865**, 65–75.
68. Park,S.J., Son,W.S. and Lee,B.J. (2013) Structural overview of toxin–antitoxin systems in infectious bacteria: a target for developing antimicrobial agents. *Biochim. Biophys. Acta*, **1834**, 1155–1167.
69. McWilliam,H., Li,W., Uludag,M., Squizzato,S., Park,Y.M., Buso,N., Cowley,A.P. and Lopez,R. (2013) Analysis tool web services from the EMBL-EBI. *Nucleic Acids Res.*, **41**, W597–W600.
70. Robert,X. and Gouet,P. (2014) Deciphering key features in protein structures with the new ENDscript server. *Nucleic Acids Res.*, **42**, W320–W324.
71. Holm,L. and Rosenstrom,P. (2010) Dali server: conservation mapping in 3D. *Nucleic Acids Res.*, **38**, W545–W549.
72. Ryter,J.M. and Schultz,S.C. (1998) Molecular basis of double-stranded RNA–protein interactions: structure of a dsRNA-binding domain complexed with dsRNA. *EMBO J.*, **17**, 7505–7513.
73. Fu,Q.Q. and Yuan,Y.A. (2013) Structural insights into RISC assembly facilitated by dsRNA-binding domains of human RNA helicase A (DHX9). *Nucleic Acids Res.*, **41**, 3457–3470.
74. Pham,T.K., Kim,D.H., Lee,B.J. and Kim,Y.W. (2013) Truncated and constrained helical analogs of antimicrobial esculentin-2EM. *Bioorg. Med. Chem. Lett.*, **23**, 6717–6720.
75. Uggerhoj,L.E., Poulsen,T.J., Munk,J.K., Fredborg,M., Sondergaard,T.E., Frimodt-Moller,N., Hansen,P.R. and Wimmer,R. (2015) Rational design of alpha-helical antimicrobial peptides: do's and don'ts. *Chembiochem*, **16**, 242–253.
76. Chen,Y.H., Yang,J.T. and Martinez,H.M. (1972) Determination of the secondary structures of proteins by circular dichroism and optical rotatory dispersion. *Biochemistry*, **11**, 4120–4131.
77. Lee,K.Y. and Lee,B.J. (2016) Structure, biology, and therapeutic application of toxin–antitoxin systems in pathogenic bacteria. *Toxins (Basel)*, **8**, 305.
78. Loris,R. and Garcia-Pino,A. (2014) Disorder- and dynamics-based regulatory mechanisms in toxin–antitoxin modules. *Chem. Rev.*, **114**, 6933–6947.
79. Svergun,D., Barberato,C. and Koch,M.H.J. (1995) CRYSOL - A program to evaluate x-ray solution scattering of biological macromolecules from atomic coordinates. *J. Appl. Crystallogr.*, **28**, 768–773.
80. Luscombe,N.M., Laskowski,R.A. and Thornton,J.M. (2001) Amino acid-base interactions: a three-dimensional analysis of protein-DNA interactions at an atomic level. *Nucleic Acids Res.*, **29**, 2860–2874.
81. Kim do,H., Im,H., Jee,J.G., Jang,S.B., Yoon,H.J., Kwon,A.R., Kang,S.M. and Lee,B.J. (2014) beta-Arm flexibility of HU from

Staphylococcus aureus dictates the DNA-binding and recognition mechanism. *Acta Crystallogr. D Biol. Crystallogr.*, **70**, 3273–3289.
82. Dey,D., Nagaraja,V. and Ramakumar,S. (2017) Structural and evolutionary analyses reveal determinants of DNA binding specificities of nucleoid-associated proteins HU and IHF. *Mol. Phylogenet. Evol.*, **107**, 356–366.
83. Cherny,I. and Gazit,E. (2004) The YefM antitoxin defines a family of natively unfolded proteins: implications as a novel antibacterial target. *J. Biol. Chem.*, **279**, 8252–8261.
84. Lah,J., Simic,M., Vesnaver,G., Marianovsky,I., Glaser,G., Engelberg-Kulka,H. and Loris,R. (2005) Energetics of structural transitions of the addiction antitoxin MazE: is a programmed bacterial cell death dependent on the intrinsically flexible nature of the antitoxins? *J. Biol. Chem.*, **280**, 17397–17407.
85. Marianovsky,I., Aizenman,E., Engelberg-Kulka,H. and Glaser,G. (2001) The regulation of the Escherichia coli mazEF promoter involves an unusual alternating palindrome. *J. Biol. Chem.*, **276**, 5975–5984.
86. Ahmad,S., Keskin,O., Sarai,A. and Nussinov,R. (2008) Protein-DNA interactions: structural, thermodynamic and clustering patterns of conserved residues in DNA-binding proteins. *Nucleic Acids Res.*, **36**, 5922–5932.
87. Andrabi,M., Mizuguchi,K. and Ahmad,S. (2014) Conformational changes in DNA-binding proteins: relationships with precomplex features and contributions to specificity and stability. *Proteins*, **82**, 841–857.
88. Spolar,R.S. and Record,M.T. Jr (1994) Coupling of local folding to site-specific binding of proteins to DNA. *Science*, **263**, 777–784.
89. Arcus,V.L., McKenzie,J.L., Robson,J. and Cook,G.M. (2011) The PIN-domain ribonucleases and the prokaryotic VapBC toxin–antitoxin array. *Protein Eng. Des. Sel.*, **24**, 33–40.
90. Kamphuis,M.B., Monti,M.C., van den Heuvel,R.H., Lopez-Villarejo,J., Diaz-Orejas,R. and Boelens,R. (2007) Structure and function of bacterial kid-kis and related toxin–antitoxin systems. *Protein Pept. Lett.*, **14**, 113–124.
91. Simanshu,D.K., Yamaguchi,Y., Park,J.H., Inouye,M. and Patel,D.J. (2013) Structural basis of mRNA recognition and cleavage by toxin MazF and its regulation by antitoxin MazE in Bacillus subtilis. *Mol. Cell*, **52**, 447–458.
92. Boggild,A., Sofos,N., Andersen,K.R., Feddersen,A., Easter,A.D., Passmore,L.A. and Brodersen,D.E. (2012) The crystal structure of the intact E. coli RelBE toxin–antitoxin complex provides the structural basis for conditional cooperativity. *Structure*, **20**, 1641–1648.
93. Dodson,G. and Wlodawer,A. (1998) Catalytic triads and their relatives. *Trends Biochem. Sci.*, **23**, 347–352.
94. Buller,A.R. and Townsend,C.A. (2013) Intrinsic evolutionary constraints on protease structure, enzyme acylation, and the identity of the catalytic triad. *Proc. Natl. Acad. Sci. U.S.A.*, **110**, E653–E661.
95. Ekici,O.D., Paetzel,M. and Dalbey,R.E. (2008) Unconventional serine proteases: variations on the catalytic Ser/His/Asp triad configuration. *Protein Sci.*, **17**, 2023–2037.
96. Chopra,N., Agarwal,S., Verma,S., Bhatnagar,S. and Bhatnagar,R. (2011) Modeling of the structure and interactions of the B. anthracis antitoxin, MoxX: deletion mutant studies highlight its modular structure and repressor function. *J. Comput. Aided Mol. Des.*, **25**, 275–291.
97. Dinh,T.T., Kim,D.H., Luong,H.X., Lee,B.J. and Kim,Y.W. (2015) Antimicrobial activity of doubly-stapled alanine/lysine-based peptides. *Bioorg. Med. Chem. Lett.*, **25**, 4016–4019.
98. Reinhardt,A. and Neundorf,I. (2016) Design and application of antimicrobial peptide conjugates. *Int. J. Mol. Sci.*, **17**, 701.
99. Kim,Y.W., Grossmann,T.N. and Verdine,G.L. (2011) Synthesis of all-hydrocarbon stapled alpha-helical peptides by ring-closing olefin metathesis. *Nat. Protoc.*, **6**, 761–771.
100. Jorgensen,M.G., Pandey,D.P., Jaskolska,M. and Gerdes,K. (2009) HicA of Escherichia coli defines a novel family of translation-independent mRNA interferases in bacteria and archaea. *J. Bacteriol.*, **191**, 1191–1199.